Plagioclase-regulated hydrothermal alteration of basaltic rocks with implications for the South China Sea rifting

Jiawang Wu [*,1], Zhifei Liu [*], Xun Yu

State Key Laboratory of Marine Geology, School of Ocean and Earth Science, Tongji University, Siping 1239, 200092 Shanghai, China

ARTICLE INFO

ABSTRACT

IODP Hole U1502B penetrates >180 m into the crystalline basement generated at a rifting margin of the South China Sea (SCS), which is the first confirmed intermediate-type margin between the magma-rich and -poor endmembers. The recovered lavas show petrographic characteristics of mid-ocean ridge basalt (MORB), but suffered pervasively from hydrothermal alteration. This sequence represents the oldest SCS oceanic crust ever drilled in-situ, and offers a globally unique window to explore the hydrothermal processes during continental breakup. Here, 50 whole-rock samples representative of Hole U1502B were analyzed for major and trace elements and Sr-Nd isotopes, presenting the first report of hydrothermally altered basalts for the SCS. The protolith appears to be tholeiite, enriched MORB, and little affected by crustal contamination due to the constant mantle-values of ε_{Nd}. However, the altered rocks are characterized by significant Ca depletion and $^{87}Sr/^{86}Sr$ modification. Major processes are identified to be tightly involved with plagioclase: chloritization and albitization. Both reactions are responsible for the Ca-loss and Sr-mobility, and for the resultant Mg- and Na-uptakes, respectively. Environments varying from the peripheral to the deep parts within a discharge zone are evidenced by the co-existence of hydro-fracturing brecciation, enrichments of base metals (Zn, Cu), high water/rock ratios

Eh (Mottl, 1983; Von Damm et al., 1985; Seyfried Jr., 1987; Bickle and Teagle, 1992; Teagle et al., 2003).

Most alterations were previously attributed to recharge zones, as documented by the effects of early subsurface alterations (Alt, 1995; Teagle et al., 2003). Thermodynamic calculations also suggest that the discharging vent fluids become compositionally fixed prior to ascending and does not attain equilibrium with surrounding rocks (Von Damm et al., 1985, 1995), because the upflow is rapid and nearly isothermal and isochemical (Ding and Seyfried Jr., 1994; Seyfried Jr. and Ding, 1995). Yet, new observations of altered crust combined with advanced modelling have shown significant extents of high-temperature reactions during the fluid upflow (Coogan, 2008). This cognition not only explains the stepped thermal gradients (i.e. from <100 °C to >250 °C) near the lava–dike transition as inferred from alteration assemblages, but also reconciles the long-standing controversy on hydrothermal fluid fluxes (e.g. Alt et al., 1986, 2010; Gillis and Robinson, 1990; Bach et al., 2003; Barker et al., 2008; Heft et al., 2008).

As the most widely used tracer of fluid–rock interaction (e.g. Albarède et al., 1981; Berndt et al., 1988; Staudigel et al., 1995; Kawahata et al., 2001; Delacour et al., 2008), however, Sr isotopes show contrasting patterns throughout the upper oceanic crust between the reference sites (e.g. Holes 504B and 1256D; Alt et al., 1986, 2010; Teagle et al., 1998, 2003; Bach et al., 2003; Barker et al., 2008; Harris et al., 2015). These discrepancies have been attributed to differences in the timing and intensity of hydrothermal alteration and associated seawater–basalt exchange fluxes (Harris et al., 2017). Such a complexity highlights the exchange of heat and fluids by faulting, at either shallow or deep levels (Haymon et al., 1991; Barker et al., 2010a; Harris et al., 2017; Tao et al., 2020).

Therefore, key issues remain unresolved principally due to a paucity of direct information, necessitating more and deeper in-situ sampling by scientific ocean drilling. Remarkably, <50 holes penetrate >50 m into lavas from normal oceanic crust, with geochemical and/or mineralogical studies done for only ~30 sites; and core recovery is typically <35% with key friable lithologies like breccia being significantly underrepresented (Staudigel, 2014; Coogan and Gillis, 2018).

Among them, much attention are placed on intermediate- to fast-spreading ridges where magmatic extension is dominant, or on slow- to ultraslow-spreading centers that are mostly hosted in ultramafic rocks; while, in between, basalt-hosted hydrothermal systems at slow-spreading ridges are rare and all characterized by complex crustal structure and deep-seated heat sources (German and Seyfried, 2014; Humphris and Klein, 2018). Firstly, the crustal structure has been recently shown to vary as competing processes of magmatic construction, dike intrusion, and hydrothermal sealing (Christeson et al., 2007, 2010; Seher et al., 2010; Gilbert et al., 2018; Estep et al., 2019). Secondly, although high-temperature hydrothermal activities are almost universally associated with the presence or inference of axial magma chamber (AMC) near the seafloor (e.g. Hannington et al., 2005; Tolstoy et al., 2008; Baker, 2009), a central role of detachment faulting has been shown for the accretion of slow-spreading oceanic crust (Boschi et al., 2006; McCaig et al., 2007; Escartín et al., 2008). Especially, the latter is thought to determine the asymmetrical accretion and concomitant hydrothermal activities at ridge segments.

In this regard, IODP Hole U1502B offers a precious window to explore the processes of hydrothermal circulation, with important

Fig. 1. Geological setting of the continent–ocean transition (COT) zone in the northern magrin of the South China Sea (SCS), showing the locations of IODP Site U1502 (yellow star) and other IODP sites mentioned in text (gray circles). a) Bathymetric map of the modern SCS, with tectonic features and three sub-basins indicated. b) Two-way traveltime (TWT) depth to the Tg acoustic basement, revealing the key basement topography: Outer Margin High (OMH) and the distinct Ridges A, B, and C (for seismic lines and profiles see Jian et al., 2018; Sun et al., 2018). Magnetic anomalies (C9, C10, and C11; red symbols) are also depicted (after Briais et al., 1993; Larsen et al., 2018a). Note that the oldest picked magnetic Chron C11n (~30 Ma) is between the Ridges A and B, seaward of Site U1502. For details see Section 2. (For interpretation of the references to color in this figure legend, the reader is referred to the web version of this article.)

Fig. 2. Lithostratigraphy of IODP Hole U1502B, with the sampled intervals shown (after Larsen et al., 2018b). Separated from sedimentary Unit V by the Tg reflecter, igneous Unit VI is divided into VIa and VIb sub-units, according to the lithology, flow morphology, and alteration style/intensity. The lithologies consist mainly of basalt, brecciated basalt, basaltic breccia, overlain by minor breccia and limestone. The morphology of lava-flow are distinguished between massive/sheet, pillow, and lobate, with the intervals of highly phyric basalts (i.e. >10% plagioclase phenocrysts) and chilled margins specified. A total of 50 whole-rock samples are categorized into 6 types based on petrographic inspections (Table S1; Figs. S1–S4), consistent with the Proceedings of IODP Expeditions 367/368 (Jian et al., 2018; Sun et al., 2018). All samples were analyzed for geochemical composition (Datasets S1–S3), and a selection of 30 samples (larger symbols) were measured for Sr and Nd isotopes (Dataset S4). In right pannel, the data of P-wave velocity (calipper data) and porosity (with inverse axis) are shown as 5-point moving average (Larsen et al., 2018b). Notably, the concurrent trends of P-wave velocity and crustal porosity data may indicate the seismic stratigraphy of Hole U1502B in the upper oceanic crust (i.e. penetration into the layer 2A/2B; also see Fig. 11). For details see Sections 3 and 4 and Supporting Information.

implications for potential interaction between magmatic and tectonic effects.

1.2. Intermediate type of rifted SCS margin and distinctive IODP site U1502

Recently, IODP Expeditions 367/368 investigated a ~100-km-long segment at the northern margin of the South China Sea (SCS), where continental breakup took place and extended seawards to the initial oceanic crust (Fig. 1). This continent–ocean transition (COT) zone was long considered as magma-poor, possibly hosting exhumed lower crust and upper mantle in its distal parts (e.g. Franke et al., 2014; Lester et al., 2014; Gao et al., 2015). The drilling, however, found mid-ocean ridge basalt (MORB) type magmatism during the breakup, and magmatic intrusion below extended crust along with widely distributed (>250 km) detachment faults (Jian et al., 2018; Sun et al., 2018). These findings are not only contrary to many expectations, but also different from any known patterns of continental breakup (cf. Whitmarsh et al., 2001; Peron-Pinvidic et al., 2013; Wang et al., 2019). Accordingly, the northern SCS margin has been suggested as the first confirmed case between the magma-rich and -poor endmembers defined by North Atlantic drilling (Larsen et al., 2018a). This intermediate-type margin may have occurred globally such as the Woodlark basin, Gulf of California, and possibly the Red Sea (Taylor et al., 1995; Lizarralde et al., 2007; Ligi et al., 2012), albeit displays a diversity depending on regional settings and evolutionary stages.

The SCS continental breakup appears to start with less magmatic extension and a highly extended margin with seaward-dipping detachment faults formed, highlighting a fast rift-to-drift transition (Larsen et al., 2018a). Magmatic additions may have intermittently intruded into the thinning continental crust, and cumulatively triggered the final breakup and onset of steady-state seafloor spreading (Larsen et al., 2018a; Ding et al., 2020). Mesozoic subductions (Taylor and Hayes, 1983; Huang et al., 2019) that made lithosphere below South China more hydrated and fractured was also proposed to precondition such fast extension, leading to enhanced diking and underplating toward the COT (Sun et al., 2019). Yet, these interpretations were conceived mostly from seismic data or coring results, with many key aspects unconstrained. In fact, the above understanding strongly relies on the distinct phenomena found at IODP Site U1502.

IODP Site U1502 drilled more than 180 m into the crystalline basement and retrieved the lavas having mid-ocean ridge basalt (MORB) compositions and petrography (i.e. plagioclase phyric) (Larsen et al., 2018b). The basalt sequence recovered from Site U1502 is unique (Fig. 2). First, it represents the oldest in-situ SCS oceanic basement ever drilled, with age no later than the early Oligocene (i.e. before ~34 Ma) as estimated from crustal seismology, magnetic anomalies, and biostratigraphy composites (Briais et al., 1993; Larsen et al., 2018a; Jian et al., 2019). Notably, its lateral equivalent of Site U1499 exhibits continental affinities (Sun et al., 2018). Second, the entire sequence experienced various degrees of hydrothermal alteration and associated brecciation. By contrast, younger and fresh basalts with similar MORB-characteristics was cored at the nearby, more seaward Site U1500 (Sun et al., 2018; Yu and Liu, 2020). In addition, Site U1502 is characterized by the plagioclase ultraphyric basalts (Cullen et al., 1989; Lange et al., 2013), while Site U1500 not.

Here, we present the first report of bulk elemental and isotopic compositions of the hydrothermally altered basaltic rocks, generated at a rifting margin of the northern SCS. To provide a representative coverage of lithologies, flow morphologies, and alteration styles (Jian et al., 2018; Sun et al., 2018), 50 samples were strategically obtained from the 182-m thick basalt sequence of IODP Hole U1502B (Fig. 2). In combination with shipboard mineralogy data (Larsen et al., 2018b), the geochemical approaches applied here – detailed Sr and Nd isotopes in particular – allow us to distinguish the alteration effects and associated fluid–rock reactions. By doing so, the hydrothermal processes and

environments can be constrained, with new insights given to the SCS marginal rifting.

2. Geological settings

2.1. Northern SCS margin

The realm from which the SCS develops was shaped by three major tectonic events: 1) compression before rifting, 2) extension during rifting, and 3) regional magma upwelling after rifting (Briais et al., 1993; Liu et al., 2017). These events caused, around the SCS basin, an active continental margin in the east, a strike-slip transform margin in the west, and a compressional margin in the south (Fan et al., 2019; Huang et al., 2019; and references therein). Such a complex setting has left the northern SCS margin the only one that was not overprinted by other processes after the breakup, thereby likely containing well-preserved geological record of the marginal rifting processes (Fig. 1).

According to magnetic anomaly records, the SCS oceanic basin formed during the early Oligocene to middle Miocene (~32–15 Ma), which can be divided into three sub-basins (i.e. East, Southwest, and Northwest; Fig. 1a), with different evolutionary histories (Taylor and Hayes, 1983; Briais et al., 1993; Li et al., 2014, 2015).

2.2. COT zone

During IODP Expeditions 367/368, seven sites spanning from a basement to the initial oceanic crust across the northern SCS margin were successfully drilled (Jian et al., 2018; Sun et al., 2018). The investigated segment (17°6′–19°2′ N, 115°2′E–117°0′ E) is characterized by a broad COT zone (~150–200 km) and a large detachment fault that separates the more stable crust landward from that of highly extended crust seaward (Fig. 1). Within the COT, seismic data reveal distinct basement highs trending SW–NE along the margin. An outer margin high (OMH) is most landward, and followed seaward by three nearly parallel ridges (i.e. Ridges A, B, and C) on a progressively thinner crust (Fig. 1b). Specifically, the crust below Ridge A is much thinner (6–8 km) than that below the OMH fault blocks (~15 km), while the crust has a uniform ~6-km thickness seaward of Ridge A (Jian et al., 2018; Sun et al., 2018, 2019; Ding et al., 2020).

In other words, the COT zone is defined by the continental OMH to the steady-state oceanic crust in Ridge C. Note that the oldest interpreted seafloor-spreading magnetic anomaly Chron C11 (~30 Ma) is between Ridges A and B (Briais et al., 1993; Larsen et al., 2018a) (Fig. 1b). Moreover, a major rifting event involving detachment faults are identified from seismic images, ending around unconformity T80 (~30 Ma), with only minor post-breakup faults affecting unconformity T60 (~26 Ma) (Larsen et al., 2018a). Therefore, sampling of basement Ridge A (i.e. Site U1502) that preserves the earliest signals of the rifting is pivotal to constrain the development of continental breakup.

2.3. IODP Site U1502

A distinct angular unconformity (Tg) separates the pre-rift and/or basement from the Cenozoic sediments on top (Figs. 1 and 2). Below the Tg, the first attempt on Ridge A failed to reach the crystalline basement but cored an undated gravel unit with silty/sandy intervals at Site U1499, overlain by condensed breccias (Sun et al., 2018). More eastwards on Ridge A, two holes were drilled at Site U1502 (Fig. 1). Hole U1502B (18°27.8798′N, 116°13.8409′E; 3763.6 m below seafloor) penetrates through the sediment/crust interface, and ~182 m into the underlying basaltic basement (739.16–920.95 m) with a core recovery of 70.7% (Fig. 2).

Shipboard analyses have shown that the U1502B lavas have MORB compositions with MORB-like petrography (i.e. plagioclase phyric, olivine-bearing, lacking clinopyroxene phenocrysts) (Larsen et al., 2018b) (Fig. 2), similar to the basalts sampled in the central SCS domain

(i.e. Sites U1431, U1433, and U1434 of IODP Expedition 349; Zhang et al., 2018) (Fig. 1). Yet, the entire U1502B basalt sequence suffered severely from hydrothermal alteration and associated brecciation. Notably, a similar MORB-characteristics but much fresher basalt unit was retrieved at nearby Site U1500 on Ridge B (Yu and Liu, 2020) (Fig. 1).

3. IODP Hole U1502B

3.1. Lithostratigraphy

Under the Tg acoustic basement, a 182-m thick sequence of aphyric to highly plagioclase porphyritic basalts, with pillow–sheet structures, was recovered in IODP Hole U1502B (Fig. 2). The lavas were heterogeneously altered by the circulation of hydrothermal fluids, as indicated by the combination of intense alteration, multiple veining, and brecciation (Table S1; Figs. S1–S5). According to lithology, flow morphology, and alteration style/intensity, the igneous Unit VI (739.16–920.95 m) is divided into two sub-units (Larsen et al., 2018b).

The lower sub-unit VIB (801.95–920.95 m) consists of aphyric to highly plagioclase phyric basalts with frequent occurrences of PUB (i.e. >10% plagioclase phenocrysts; Cullen et al., 1989; Lange et al., 2013) (Fig. 2). A coherent series of sheet and lobate lava flows prevails the VIB, with interbedded pillows. Pillow basalts are identified by chilled margins and/or pillow rims, which appear to be glassy prior to the alteration, considering the very fine grain size, and the perlitic cracking and quenching textures (Gregg and Fink, 1995; Kennish and Lutz, 1998). The alteration phases are dominated by chlorite, epidote, and sulfides, with accessory minerals like clay minerals, zeolites, carbonates, and opaque minerals (Larsen et al., 2018b) (Table S1; Figs. S2 and S3).

The upper sub-unit VIa (739.16–801.95 m) is characterized by a sequence of brecciated and fractured massive lava flow, with minor chert and claystone (Fig. 2). The VIa breccia clasts of plagioclase phyric basalts are petrologically like those in VIb; the matrix is composed

6

Fig. 3. Downhole profiles of selected proxies for the hydrothermally altered basaltic rocks of IODP Hole U1502B. Lithostratigraphy is shown relative to the Tg reflector (i.e. in oceanic basement; see Fig. 2), and different types of samples are distinguished (see Section 3). Fe$_2$O$_3$* refers to total iron oxides; the data of loss on ignition (LOI) and the water/rock (W/R) ratio estiamted from Sr isotopes systematics are also plotted. For reference, the SCS basalts sampled by IODP Expeditions 367/368 on the same rifted margin (Sites U1500; Yu and Liu, 2020), and by Expeditions 349 on the spreading seafloor (Sites U1431, U1433, and U1434; Zhang et al., 2018) are compared (see Fig. 1), in addition to the global MORB (Gale et al., 2013).

4. Sampling and analyses

A total of 50 whole-rock samples were strategically selected from Hole U1502B for geochemical analyses, covering most – if not all – of the lithologies, flow morphologies, and alteration/mineralization styles (Larsen et al., 2018b) (Fig. 2; Table S1). The alteration degree as well as the primary and secondary mineralogy were assessed by visual core/ sample description (Fig. S1) and thin section examination (Figs. S2–S4). The samples are classified into three main categories according to the alteration effects: 1) relatively fresh, 2) hydrothermally altered, and 3) affected by brecciation. On that, six sample-types are further specified.

Fractured basalt without any matrix between the basaltic fragments is described as basalt, and divided into "relatively fresh basalt", "highly altered basalt", and "fully altered basalt", according to the degree of alteration (Figs. S1–S3). Note that the samples with abundant plagioclase phenocryst are occasionally differentiated in text. Relatively fresh basalt refers to those samples altered moderately, and its primary texture is not apparently changed. The "fully altered basalt" denotes the three samples containing >90% secondary and veining minerals with no sign of brecciation, which may be useful as hydrothermal alteration endmembers. In between, the other samples that were not affected by brecciation are labelled as "highly altered basalt".

Depending on the intensity of fragmentation and ratio of clast/matrix, the brecciated samples are distinguished (Figs. S1 and S4): highly fractured, matrix-supported intervals and intervals with a mixture of basaltic and sediment clasts are defined as "basaltic breccia"; intervals that are fractured but clast-supported are defined as "brecciated basalt". In addition to the samples from igneous Unit VI, one "breccia" sample is taken from the overlying sedimentary Unit V for reference. Note that our observation-oriented sample classification (Fig. 2; Table S1) is well consistent with the criteria in the Proceedings of IODP Site U1502 (Larsen et al., 2018b), and confirmed by the final geochemical results.

All 50 samples were analyzed for major and trace elements by X-ray fluorescence (XRF) and ICP-MS (i.e. inductively coupled plasma - mass spectrometry), showing the relative standard deviations of <4% and <10%, respectively (Datasets S1–S3). A sub-set of 30 samples were further determined for radiogenic Sr and Nd isotopes on a Neptune Plus multi-collector ICP-MS, giving the 2σ external errors of 18 ppm and 19 ppm, respectively (Dataset S4). For analytical details see Supporting Information.

5. Results

To provide a framework for interpretations of the geochemical variations, a lithostratigraphic summary for Hole U1502B is presented in Fig. 2, with the sampled intervals shown. For detailed accounts of the alteration characteristics see Section 3. Sample descriptions based on the visual assessment and microscopic checks in this study and on shipboard are compiled in Supporting Information. Downhole profiles of major elements, $^{87}Sr/^{86}Sr$ and ε_{Nd}, and selected proxies including LOI, Ce/Pb,

Fig. 4. Geochemical discrimination for the protolith of IODP Hole U1502B: a) plot of total alkalis (Na$_2$O + K$_2$O) vs. SiO$_2$ (Macdonald and Katsura, 1964); b) plot of V vs. Ti (Shervais, 1982), compared with the reference data of MORB (Gale et al., 2013), IAB (Labanieh et al., 2012), and OIB (Chauvel et al., 2011); and c) incompatible element pattern normalized to primitive mantle (Sun and McDonough, 1989). For the sample-types of Hole U1502B see Fig. 2. Sources of reference data refer to the caption of Fig. 3.

Nb/Zr, Mg/Ca, W/R ratio are plotted in Fig. 3.

5.1. Protolith composition of Hole U1502B

A set of 12 "relative fresh basalt" samples appears to be least affected by hydrothermal alteration, thereby likely retaining the original geochemical composition (Fig. 2). These samples have basaltic abundance of SiO_2 (49.38 ± 1.56%) and typically low alkali elements (Na_2O: 3.25 ± 0.40%; K_2O: 0.24 ± 0.16%), which are plotted within the tholeiite field on the classification of ($Na_2O + K_2O$) vs. SiO_2 (Macdonald and Katsura, 1964) (Fig. 4a). The V-Ti discrimination plot (Shervais, 1982) further suggests a MORB composition for the protolith of Hole U1502B (Fig. 4b). This is confirmed by the multi-element diagram normalized to primitive mantle (Sun and McDonough, 1989), indicating a type of enriched MORB (i.e. E-MORB) (Fig. 4c).

In fact, these relatively fresh samples of Hole U1502B show similar major-element composition to the fresh basalts cored at the same rifted margin (Site U1500; Yu and Liu, 2020), the seafloor basalts collected from the central SCS basin (Sites U1431, U1433, and U1434; Zhang et al., 2018), and the global MORB (Gale et al., 2013) (Figs. 3a–e and 4); the only exception is the highly depleted CaO contents (Fig. 3d). On the contrary, the samples affected by alteration and brecciation diversely deviate from the fresher basalts of Hole U1502B and from the scopes defined by reference data (Figs. 3 and 4).

5.2. Chemical mobility related to alteration

The most distinct feature in Hole U1502B is the strong loss of CaO (Fig. 3d). By contrast, considerable enrichments are observed in Fe- and Mn-oxides, except for some of the brecciated samples in sub-unit VIa (Fig. 3b). Particularly, there are prominent enrichments of base metals like Zn and Cu throughout Hole U1502B (Fig. 3g;).

Distinguished between the altered and brecciated samples, data of Hole U1502B are normalized to the global MORB (Gale et al., 2013) to show enrichment/depletion of the elements (Fig. 5a–b). The basaltic rocks display nearly flat curves with elemental abundances close to 1.0 unity for the rare earth elements (REE) and high-field strength elements (HFSE; e.g. Zr, Hf, Ti, Y, Nb), reflecting their conservative properties to hydrothermal alteration (Fig. 5a–b). By contrast, large variations mainly occur in the relatively incompatible elements, especially the large-ion lithophile elements (LILE) such as Cs, Rb, Ba, K, Pb, and Sr (Fig. 5a–b).

Moreover, the trends of chemical mobility differ between the types of samples. Enrichments in Th, U, Pb, and Sr, with Rb and Ba depletions are observed for the samples hydrothermally altered alone (i.e. altered samples) (Fig. 5a). While for the samples affected also by brecciation (i.e. brecciated samples), enrichments in Ba, U, K, Pb, Sr, and Zr, with Nb and Ti depletions are seen (Fig. 5b). Consequently, the brecciated samples contain consistently high Zr and Ba and low Ti contents relative to the altered samples (Fig. 5a, b), causing distinctly lower values of Nb/Zr in the sub-unit VIa than VIb (Fig. 3h). More specifically, the samples of brecciated basalt have higher Zr and Ba contents than those of basaltic breccia (Fig. 5b).

The REE fractionation pattern with normalization to chondrite (Anders and Grevesse, 1989) are also presented (Fig. 5c–d). Unlike the reference MORB data, most of U1502B samples show enrichment of light REE (LREE) relative to heavy REE (HREE). Besides, some samples have positive Eu anomaly (i.e. Eu/Eu* > 1) that are typical of the plagioclase-involved hydrothermal processes (Klinkhammer et al., 1994; Douville

Fig. 5. Trace element patterns for the hydrothermally altered basaltic rocks of IODP Hole U1502B: incompatible element patterns normalized to global MORB (Gale et al., 2013), arranged in the order of ascending compatibility (Sun and McDonough, 1989) (left panel); and REE (i.e. rare earth element) fractionation patterns with normalization to chondrite (Anders and Grevesse, 1989) (right panel). Comparisons of the relatively fresh basalts with the samples affected by hydrothermal alteration alone (a, c), and with the samples also affected by hydro-fracturing brecciation (b, d). Sources of reference data refer to the caption of Fig. 3.

Fig. 6. Close correspondences with LOI and $^{87}Sr/^{86}Sr$ data permit the use of Ce/Pb and Nb/U ratios as reliable proxies of alteration degree in IODP Hole U1502B. The basalt samples that were not apparently affected by hydrothermal alteration are identified, i.e. those with LOI <5.5% and $^{87}Sr/^{86}Sr$ <0.7048. For the sample-types of Hole U1502B see Fig. 2. Sources of reference data refer to the caption of Fig. 3.

Fig. 7. Plot of ε_{Nd} vs. $^{87}Sr/^{86}Sr$ of the hydrothermally altered basaltic rocks of IODP Hole U1502B. Sources of the reference data: SCS seafloor basalts (i.e. Sites U1431, U1433, and U1434; Zhang et al., 2018), global and Pacific MORB (Gale et al., 2013), and lower CC (i.e. lower continental crust) of South China (Dai et al., 2008); and averaged data of Hainan OIB (after Zhang et al., 2018) and SCS seamounts (after Zhong et al., 2018). Variations in $^{87}Sr/^{86}Sr$ point to a pervasive hydrothermal alteration, which has little affected the mantle-derived, nearly invariable ε_{Nd} values. The hydrothermal fluids appear to evolve in ambient seawater of late-Eocene age (global seawater $^{87}Sr/^{86}Sr$ signature: 0.7078 $\pm$ 0.0001; McArthur et al., 2012).

et al., 1999) (Fig. 5c–d).

Ratios of incompatible elements such as Ce/Pb and Nb/U are widely employed as sensitive indicators of crustal contaminants on the mantle-derived substances (Hofmann et al., 1986; Rehkämper and Hofmann, 1997). In our case, the close correspondence with LOI data permits the use of Ce/Pb and Nb/U ratios as reliable proxies of alteration degree (Fig. 6a, b). The alteration degree as proxied by Ce/Pb exhibits a gradual decrease downhole U1502B (Fig. 3i), which is consistent with the macro- and microscopic views (Larsen et al., 2018b) (Section 3; also see Supporting Information). Being sample type specified, the data distribution as observed in Fig. 6 agrees well with our sample classification (Fig. 2). For instance, the typically high, mantle values only correspond to the samples with LOI <5.5% and $^{87}Sr/^{86}Sr$ <0.7048, indicating the primitive basalts in Hole U1502B (Fig. 6a–d). Likewise, the plot of Nb/U vs. Ce/Pb neatly isolates the samples that were little affected by hydrothermal alteration and brecciation (Fig. 6e).

5.3. Radiogenic isotopes of Sr and Nd

Except the breccia sample (ε_{Nd}: −7.2 ± 0.2) from the overlying sedimentary unit, the basaltic rocks of Hole U1502B show mantle ε_{Nd} signatures (+7.1 to +9.4 ± 0.2) (Figs. 3l and 7). These values are within the ranges of the global MORB (Gale et al., 2013) and the SCS oceanic crust as delimited by Sites U1431, U1433, and U1434 near the fossil spreading ridges (Zhang et al., 2018). Moreover, the small ε_{Nd} variations and the nearly constant Nd and Sm concentrations in Hole U1502B basalt sequence appear insensitive to alteration and brecciation (Figs. 5 and 7).

On the contrary, variability of Sr isotopes indicates a seawater-fueled hydrothermal alteration, with the evolved fluids likely sourced from late-Eocene seawater (McArthur et al., 2012) (Figs. 3m and 7). For most of the samples, the positive, hyperbola-like relationships between LOI and 1000/Sr values and $^{87}Sr/^{86}Sr$ ratios reflect higher permeability or more heavily altered sample (Fig. 8a, b). This is especially apparent in the "fully-altered" samples with macroscopically zoned alteration domains. Besides, there is a separate trend observed for the samples affected by brecciation in the diagrams of LOI and 1000/Sr vs. $^{87}Sr/^{86}Sr$ (Fig. 8a, b).

Using $^{87}Sr/^{86}Sr$ as a tracer of fluid–rock interaction, the alteration linked to different mineralogical reactions such as chlorite, albite, sericite, and epidote can be discerned (Figs. 8b–d and 10). In addition, the Ca–Mg–Na–Sr correspondences permit the major alteration effects to be distinguished (Figs. 9 and 10).

5.4. Estimate of water/rock (W/R) ratio

Water/rock (W/R) ratio quantified with Sr isotopes systematics is widely applied to indicate the extent of fluid–rock interaction in crustal sections (Albarède et al., 1981). Assuming the final isotope equilibrium of Sr isotopes, the fluid–rock interaction can be described by the simple mass balances for closed system and open system, respectively, as follows. (cf. Berndt et al., 1988; Kawahata et al., 2001; Delacour et al., 2008).

$$W \ R \ ratio\,(closed\,system) = \left(Sr^{i}_{rock} - Sr^{f}_{rock} \right) \Big/ \left(Sr^{f}_{rock} - Sr^{i}_{water} \right) * \left(Sr_{rock}/Sr_{water} \right)$$

$$W \ R \ ratio\,(open\,system) = ln\left[\left(Sr^{i}_{rock} - Sr^{f}_{rock} \right) \Big/ \left(Sr^{f}_{rock} - Sr^{i}_{water} \right) + 1 \right] * \left(Sr_{rock}/Sr_{water} \right)$$

Therein, W is the mass of hydrothermal fluid, R is the mass of rock being altered; $\varepsilon Sr^{i}_{rock}$ and $\varepsilon Sr^{f}_{rock}$ is the initial and final isotopic ratio of rock, respectively; $\varepsilon Sr^{i}_{water}$ and $\varepsilon Sr^{f}_{water}$ is the initial (i.e. seawater) and final isotopic ratio of fluid, respectively. Note that $\varepsilon Sr^{f}_{rock}$ is equal to $\varepsilon Sr^{f}_{water}$; Sr_{rock} and Sr_{water} is the Sr concentration of unaltered rock and of seawater, respectively. The values of $\varepsilon Sr^{i}_{rock}$ ($^{87}Sr/^{86}Sr$: 0.70309) and Sr_{rock} (Sr: 168 ppm) after the mean values of Site U1500 basalts (Yu and

Liu, 2020) and SCS seafloor basalts (i.e. Sites U1431, U1433, and U1434; Zhang et al., 2018), and the values of $\varepsilon Sr^{f}_{water}$ ($^{87}Sr/^{86}Sr$: 0.70780; McArthur et al., 2012) and Sr_{water} (Sr: 12 ppm; Antonelli et al., 2017) after the global seawater estimates of the late-Eocene age.

Closed system, or "single-pass" models assume that all the unreacted fluid enters the system (i.e. rock) as a single event, equilibrates with the rock and then leaves the system. By contrast, open system, or "multipass" models are time-integrated models that assume infinitesimally small aliquots of fluid enter the rock, equilibrate, and then leave the system before the next aliquot reacts with the rock. Considering the variable environments of discharge zone as discussed below, the estimate of open-system W/R ratios is more appropriate for the case of Hole U1502B (Figs. 3n and 9i). For the W/R-ratio results and associated details see Dataset S4.

6. Discussion

The hydrothermally altered basaltic rocks of IODP Hole U1502B are characterized by the significant depletion of CaO (Fig. 3), which contains key messages on alteration reactions and hydrothermal processes. As frequently substituted for Ca, Sr is known to participate in most magmatic, lithospheric, and secondary processes, especially hydrothermal alteration (Blundy and Wood, 1991; Berndt and Seyfried Jr., 1993; Klinkhammer et al., 1994). Moreover, radiogenic Sr isotopes have been proven a powerful tracer for fluid–rock interaction within MOR environments because the $^{87}Sr/^{86}Sr$ ratios of seawater and fresh oceanic crust are distinctly different and there is neither temperature- nor mineral-dependent isotopic fractionation of Sr (Albarède et al., 1981; Berndt et al., 1988; Kawahata et al., 2001; Delacour et al., 2008). Besides, Sr mobility in the presence of fluid at greenschist facies conditions is thought to promote the isotopic exchange, but also dependent on the mineralogical reactions occurring (Bickle and Teagle, 1992; Bach et al., 2003; Teagle et al., 2003; Gillis et al., 2005; Barker et al., 2008; Harris et al., 2015). Therefore, the knowledge of how Sr systematics behaves with respect to the loss of Ca is crucial to 1) unravel the hydrothermal processes and determine the first-order control on alteration effects, and 2) constrain the hydrothermal environments and crustal evolution prevailed within the SCS rifting margin.

After characterizing the hydro-fracturing brecciation, the strong Ca loss can be mostly attributed to plagioclase-regulated alterations, with albitization and chloritization identified to be responsible for the Ca-Na and Ca-Mg exchanges respectively (Section 6.1). We assess the variable environments representative of a discharge zone, and further suggest that Hole U1502B may have penetrated a mixing zone of hydrothermal fluid and seawater that is likely within the lava–dike transition (Section 6.2). Finally, we propose a conceptual model to incorporate most existing results, highlighting the seismic layer 2A/2B boundary and the fault-hosted hydrothermal upflow channels, with implications for the SCS marginal rifting (Section 6.3).

6.1. Identifying alteration processes

6.1.1. Hydro-fracturing induced brecciation

The basalt sequence of Hole U1502B exhibits overall homogenous, mantle ε_{Nd} values (+7.1 to +9.4 ± 0.2), within the ranges of seafloor basalts recovered from the central SCS basin (Zhang et al., 2018) and of the globally averaged MORB (Gale et al., 2013) (Figs. 3l and 7). This suggests that the Nd isotope composition remains unaffected by hydrothermal alteration and subsequent seafloor weathering (Michard et al., 1983; Michard and Albarède, 1986; Staudigel et al., 1995; Wu et al., 2018). In turn, the nearly identical ε_{Nd} values between brecciated and non-brecciated samples corroborate that the breccia-clasts in Site U1502 were mostly sourced from the same basalts, rather than of sedimentary origin (Larsen et al., 2018b). Moreover, the primitive basalts in Hole U1502B can be further isolated by Ce/Pb and Nb/U as indicators of crustal influence (Hofmann et al., 1986; Rehkämper and Hofmann,

Fig. 8. Plots using Sr isotopes systematics ($^{87}Sr/^{86}Sr$ and Sr) as a tracer of fluid–rock interaction to unravel the alteration effects and hydrothermal processes occurred in IODP Hole U1502B. The LOI data are used to reflect the degree of alteration, representing the amounts of secondary hydrous minerals (a). Using 1000/Sr and Ca/Sr, the cumulative effects of plagioclase alterations can be distinguished from that of hydro-fracturing brecciation (b, c). The decreasing Ca/Sr ratios point to epidote formation; and the steady state refers to the reactions with high W/R ratio and temperature (c). Brecciation may have promoted the alteration degree by enhancing W/R ratio (a–c). Na/Mg is taken to further trace the relative extents of albitization and chloritization (d). The evolved fluids appear to be sourced from the seawater of late-Eocene age (global seawater $^{87}Sr/^{86}Sr$ signature: 0.7078 ± 0.0001; McArthur et al., 2012). For the sample-types of Hole U1502B see Fig. 2. Sources of reference data refer to the caption of Fig. 3.

1997), showing that the typically high, mantle-derived ratios only correspond to those with LOI <5.5% and $^{87}Sr/^{86}Sr$ <0.7048 values (Fig. 6a–d). This is further delimited by the regional and global MORB references (i.e. Gale et al., 2013; Zhang et al., 2018; Yu and Liu, 2020) (Fig. 6e).

Being lithologically specified, the samples affected by brecciation have generally higher LOI and $^{87}Sr/^{86}Sr$ values than those altered hydrothermally alone, revealing that the alteration effects must have been promoted by brecciation (Fig. 8a, b). This confirms the nature of brecciation, i.e. the formation of breccias involved fluid-assisted fracturing, related to the hydraulic and in-situ fragmentation of basalts (Larsen et al., 2018b). Such rocks are commonly described in hydrothermal systems (Delaney et al., 1987; Saccocia and Gillis, 1995; Jébrak, 1997).

There appears to be a bifurcation starting around 0.7055–0.7060 of $^{87}Sr/^{86}Sr$, coinciding to the lower CC signature of the South China (Dai et al., 2008) (Fig. 8). The bifurcating trends point to not only the promoting effects of alteration due to enhanced W/R ratios (Fig. 9i), but also the possible crustal additions with distinct compositions caused by brecciation, i.e. toward the late-Eocene global seawater (McArthur et al., 2012) vs. toward the overlying breccia (Fig. 8a, b).

Indeed, although the brecciation mostly prevails in sub-unit VIa and commonly exhibit increased Zr and decreased Ti contents (Fig. 5b), a closer examination suggests multiple events – rather than a single stage – of brecciation. Firstly, the breccia endmember taken from overlying sedimentary unit does not necessarily correspond to the trends of brecciation effect (Figs. 8a, b and 9e). Secondly, considerably lower Nb/Zr and Ti/Zr values are observed in the lower part of VIa, close to the VIa–VIb boundary, causing the diverse changes associated with brecciation (Fig. 3h; also see Supporting Information). Thirdly, the brecciated basalts with consistently higher Zr and Ba contents than the basaltic breccias – instead of the other way around – indicates that there must be different sources of breccia (Fig. 5b). In other words, the different compositions and trends indicate that there must be different sources of breccia or the heterogenous nature.

This inference is supported by the possible presence of faulting breccia around the boundary of VIa and VIb sub-units. Macroscopic observations suggest a gradual increase of the brittle deformation passing from a clast-supported cataclastic fabric to a matrix-supported fault gouge (Fig. S5). Yet, the identification of characteristic microstructures resulting from shear deformation is precluded by a pervasive fluid circulation associated with replacement, destabilization, and recrystallization of the initial texture (cf. Larsen et al., 2018b). These together may suggest a mixture of two mechanisms regarding the breccia formation in Hole U1502B, i.e. hydrothermal and tectonic, reflecting a complex history of SCS marginal rifting (see Section 6.3.1).

6.1.2. Plagioclase-regulated alteration

After characterizing the brecciation, we can further explore the first-order processes of hydrothermal alteration occurred in Hole U1502B. At the first glance, the heavy Ca loss from the altered basalts (Fig. 3d) could be linked to the formation of anhydrite ($CaSO_4$). Anhydrite precipitates

(caption on next column)

Fig. 9. Plots of diagnostic proxies for the hydrothermal processes occurred in the basaltic rocks of IODP Hole U1502B. For the sample-types of Hole U1502B see Fig. 2. Sources of reference data refer to the caption of Fig. 3. For interpretations see Sections 6.1 and 6.2.

from seawater at temperatures above ~130 °C because of its retrograde solubility (Bischoff and Seyfried Jr., 1978). This process essentially removes all Ca and ~33% of SO$_4$ from seawater, leading to additional Ca leached from host rocks (Humphris and Thompson, 1978; Seyfried Jr., 1987). In general, almost all the Ca in high-temperature seafloor hydrothermal fluids is derived from the rocks (cf. Antonelli et al., 2017).
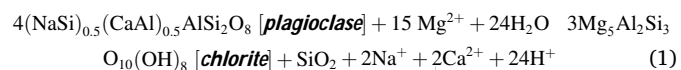
However, lines of evidence argue against the predominance of anhydrite precipitation. Firstly, there is no sign of the presence of anhydrite in Hole U1502B, while the abundant pyrite indicates that the hydrothermal fluids were rich in sulfur (Larsen et al., 2018b) (see Section 3.2). High barite contents in some of the brecciated samples may support the availability of dissolved sulfate (Fig. 5a, b). Secondly,

although the distribution and abundance are still controversial (Sleep, 1991; Barker et al., 2010b), it is generally recognized that anhydrite forms early in the upflow limb of hydrothermal circulation, mostly within the recharge zone (Tivey, 2007; Alt et al., 2010; Humphris and Klein, 2018). A massive precipitation of anhydrite thus conflicts with the strong evidence pointing to a discharge zone inferred for Hole U1502B (see Section 6.2.1). Thirdly, anhydrite has a large capacity to reduce Sr content in fluid, which would cause a relevant loss of Sr in altered rocks, as suggested by the studies of crustal sections (Teagle et al., 1998; Gillis et al., 2005; Barker et al., 2008). However, this is not the case for Hole U1502B (Fig. 8b, c).

Alternatively, the loss of Ca and associated Sr mobility in altered

oceanic crust are widely linked to plagioclase (cf. German and Seyfried, 2014). As a key phase, the crystal chemistry of plagioclase is thought to influence the reactivity of the crust, and the partitioning of trace elements (Blundy and Wood, 1991). Supported by the MORB petrography of Hole U1502 (see Section 2.3 and Supporting Information), our results demonstrate two major processes of hydrothermal alteration.

6.1.2.1. Chloritization. Apart from the sulfate removal, the MOR hydrothermal circulation is dominated by the exchange of seawater Mg for basaltic Ca through the transformation of primary igneous minerals to alteration phases (cf. Humphris and Klein, 2018). As seawater penetrates deeper and is heated to temperatures above ~150 °C, the Ca-Mg exchange occurs mainly on plagioclase, resulting in the precipitation of clay minerals at different temperatures; Mg-rich smectite form at ~150–200 °C and chlorite formation prevails at >200 °C (Alt et al., 1986; Alt, 1995). In addition, the Mg-rich mineral tremolite could be rapidly precipitated once sufficient Ca, Al, and Si are provided by dissolution of plagioclase and pyroxene (German and Seyfried, 2014). These processes are facilitated at higher temperature and can be primarily represented by Reaction 1 for chlorite formation (after Mottl, 1983; Tivey, 2007), showing that the uptake of Mg by the rocks is roughly balanced with respect to electrical charge by leaching of Ca^{2+} and Na^+ cations.

$$4(NaSi)_{0.5}(CaAl)_{0.5}AlSi_2O_8\ [\textbf{\textit{plagioclase}}] + 15\ Mg^{2+} + 24H_2O\ \ 3Mg_5Al_2Si_3$$
$$O_{10}(OH)_8\ [\textbf{\textit{chlorite}}] + SiO_2 + 2Na^+ + 2Ca^{2+} + 24H^+ \qquad (1)$$
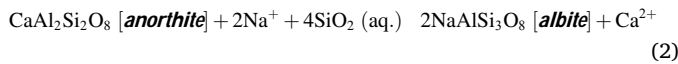
This so-called chloritization is known to influence not only the release of Ca and Sr from basaltic substrates into hydrothermal fluids, but also the generation of acidity. Experiments suggest that low pH cannot be maintained when Mg^{2+} is effectively removed from solution, as the H^+ ions produced by Reaction 1 are rapidly consumed by silicate hydrolysis (Mottl, 1983). But this is different from the acidic vent fluids as commonly found (Von Damm et al., 1985; German and Seyfried, 2014). In effect, it is the high Ca from dissolution of plagioclase that buffers pH and meanwhile accounts for a complete exchange of Mg for Ca (Berndt and Seyfried Jr., 1993; Seyfried Jr. and Ding, 1995; Antonelli et al., 2017).

In Hole U1502B, the prevalence of chloritization is evidenced by the abundant chlorite (5–30%) in bulk mineralogy (Larsen et al., 2018b) (see Section 3.2), and by the tight correspondence between the Mg enrichment (i.e. Mg/Ca) and the W/R ratio estimated from Sr isotopes (Fig. 9i). The effects can be seen from the negative relationships of MgO–CaO and MgO–SiO₂ (Fig. 9b, d) and in the ternary space of Ca–Sr–Mg (Fig. 10b) on bulk composition. Alteration of oceanic basalts usually shows a negative correlations l   eceen

Tivey, 2007) (Fig. 9a). The albitization is a widespread ion exchange reaction through alteration of anorthite (An) to albite (Ab), and can be approximated by Reaction 2 (after Berndt and Seyfried Jr., 1993; Mottl et al., 2011). Thermodynamic calculations suggest that albite starts to form at temperature >220–300 °C, and the extent of Na-fixation decreases with increasing temperature due to a decrease in the equilibrium constant in Reaction 2 (Seyfried Jr. et al., 1988). Note that Na does not simply replace Ca in plagioclase but is rather buffered along with Ca by plagioclase–fluid equilibria (Berndt and Seyfried Jr., 1993).

The negative Ca–Na correlation is especially clear after excluding the brecciated samples, while the variability between them – especially (e.g. manifested in Zr [ppm]/SiO$_2$) may reflect the heterogeneous of this reaction (Fig. 9a). In fact, the partial alteration of plagioclase throughout Hole U1502B – such as the common signs of albitized plagioclase – is clearly reflected by the concurrent changes of Na, Al, and Si in bulk composition (see Section 3.2 and Supporting Information). The relict igneous plagioclase has relatively low An content (i.e. labradorite, 50–70% of An content), which is likely resulted from an accretion of hydrothermally albitized plagioclase with <20% An content (e.g. Gillis et al., 2005), as fresh MORB typically contains plagioclase with An content >75% (Blundy and Wood, 1991; Yu and Liu, 2020).

$$CaAl_2Si_2O_8\ [\textbf{\textit{anorthite}}] + 2Na^+ + 4SiO_2\ (aq.)\ \ 2NaAlSi_3O_8\ [\textbf{\textit{albite}}] + Ca^{2+}$$
(2)

It has been demonstrated that the partitioning of Sr between plagioclase and fluid is primarily dependent upon the process of albitization (Berndt et al., 1988; Seyfried Jr. et al., 1988, 1991; Berndt and Seyfried Jr., 1993). The extent of albitization is evidenced by the positive correlations between Sr/Zr and Na/Zr (Fig. 9g) and by the tight correspondence in the Ca–Sr–Na ternary space (Fig. 10a), being consistent with experimental predictions (Berndt et al., 1988, 1989; Blundy and Wood, 1991).

Furthermore, the LREE enrichment and positive Eu anomaly as observed in Hole U1502B (Fig. 5c, d) are diagnostic of the REE partitioning caused by chemical substitution for Ca and Sr under greenschist facies alteration (Klinkhammer et al., 1994; Douville et al., 1999). In particular, the negative relationship between Na/Sr and Eu/Eu* (Fig. 9h) suggests a transition from An-rich igneous plagioclase to Ab-rich hydrothermal plagioclase. Combined with the highly positive correlation of Na-Sr that is normalized to the generally immobile element Zr (Humphris and Thompson, 1978; Fowler and Zierenberg, 2016), this indicates a major role of albitization (Figs. 9g and 10c). Such plagioclase-involved hydrothermal processes are widely found in the high-temperature venting fluids of basalt-hosted hydrothermal systems (e.g. Michard et al., 1983; Michard and Albarède, 1986; Klinkhammer et al., 1994; Douville et al., 1999; Pester et al., 2012).

6.1.3. Plagioclase-regulated alteration features

On the other hand, magmatic differentiation is unlikely to retain a detectable effect on the results as interpreted above. Firstly, the plagioclase (-Pl) and clinopyroxene (-Cpx) fractionations cannot account for the slightly negative trend between MgO and CaO contents, as observed for the samples of relatively fresh basalt sample (Fig. 9b). Indeed, limited clinopyroxene fractionation has been reported for the fresh MORB at nearby Site U1500 (Yu and Liu, 2020), which may be a magmatic feature for the early SCS marginal rifting. Secondly, although the MgO–CaO distribution may be linked to olivine fractionation (-Ol), the lack of MgO–SiO$_2$ correlation for the relatively fresh basalts excludes this possibility (Fig. 9d), as olivine fractionation would increase the SiO$_2$ and Al$_2$O$_3$ contents and decrease MgO contents. Besides, the Na$_2$O content has a close correspondence with CaO (i.e. the focus of our discussion), but appears not to be influenced by magmatic differentiation since there is no discernable negative relationship between Na$_2$O and MgO for the samples of relatively fresh basalt (Fig. 9c).

In fact, our interpretation on plagioclase-regulated alteration in Hole U1502B is fully consistent with its MORB petrography, having plagioclase phyric, olivine-bearing, no clinopyroxene phenocrysts (see Section 3 and Supporting Information). Experiments on plagioclase alteration have suggested that albitization is facilitated by interaction with the fluids containing high Na/Mg ratio and SiO$_2$ (aq.) contents (Seyfried Jr. et al., 1988; Seewald and Seyfried Jr., 1990). Chlorite precipitation leads to Mg-poor, and Na- and Si-rich hydrothermal solutions (Reaction 1), thereby promoting the albite-forming reaction (Reaction 2). In other words, the former reaction provides a source of H$^+$ ion and buffers Ca/Sr ratios of the fluids (Berndt et al., 1988, 1989; Figs. 8 and 10).

Plagioclase is the primary reservoir for Sr in the upper oceanic crust. Replacement of primary plagioclase can lead to variable effects on the whole-rock Sr composition, dependent on the secondary phase formed. On the contrary, pyroxene alteration, if any – is unlikely to have effect on Sr-uptake (Gillis et al., 2005). Studies designed to investigate mineralogical control on

Teagle, 1992).

The inference of discharge zone seems to conflict with the extremely high W/R ratios (~1–25) as estimated from the Sr isotopes systematics for Hole U1502B (Figs. 3n and 9i). The quartz–pyrite cemented breccias also suggest a near-surface, high-W/R interaction (Delaney et al., 1987; Saccocia and Gillis, 1995). This discrepancy can be explained by seawater entrainment. In the core of discharge zone, where hydrothermal fluids rise without mixing with seawater, seritization (i.e. plagioclase replaced by sericite) and silicification dominate (Humphris and Klein, 2018). Therein, SiO_2 becomes saturated but does not precipitate due to kinetic barriers at the low pH of the ascending fluids; and minor amounts of precipitation and/or dissolution of sulfide phases may occur (Ding and Seyfried Jr., 1994; Von Damm et al., 1995; Tivey, 2007). As the fluids rise and become cooler, both quartz and sulfides precipitate, enhancing the leaching of Mg and Ca from the rocks. In the peripheral parts of discharge zone, on the other hand, occasional entrainments of seawater should have provided a source of Mg to the ascending fluid, but caused a removal of Ca and alkalis from the rocks, with W/R ratios as high as >50 (Humphris and Thompson, 1978; Mottl, 1983; Bach et al., 2013). With resemblance to the classical Troodos ophiolite (e.g. Schiffman and Smith, 1988; Gillis and Robinson, 1990), this explanation can largely account for the assemblages of chlorite + quartz + pyrite ± sericite and the associated Mg enrichment in Hole U1502B (Fig. 9i).

However, this scenario most likely occurs in the shallower parts of discharge zone (Mottl, 1983; Bach et al., 2013; Humphris and Klein, 2018) and cannot explain the prevalence of albitization in Hole U1502B that are indicative of low W/R-ratio conditions and deep reactions (Figs. 8 and 10). Indeed, the greenschist facies mineral assemblage of albite + chlorite + epidote indicates high-temperature (>250–450 °C) fluid–rock interactions (Reyes, 1990; Franzson et al., 2008; Staudigel, 2014). The presence of epidote + quartz ± chlorite reflects what remains of basalt exposed repeatedly to upwelling fluids, which is representative of the deepest parts of hydrothermal systems preserved in ophiolites (Alt, 1995; Banerjee et al., 2000; Gillis et al., 2001; Barker et al., 2010a; Bach et al., 2013) or in the well-developed stockwork beneath vent fields (e.g. the largest active hydrothermal mound TAG; Hannington et al., 2005; Tivey, 2007).

Moreover, the observation that epidote is often associated with albitized plagioclase (see Supporting Information) suggests that reactions with high temperature and high W/R ratio (Fowler and Zierenberg, 2016; Fox et al., 2020); while that the albitization is locally facilitated by chloritization (Figs. 8c, d and 10) suggests reactions with highly evolved, upwelling fluids (Seyfried Jr. et al., 1988). A combination of these two may indicate that Hole U1502B was located once close to the reaction zone and/or the hydrothermal conduits.

This inference is supported by the common features of prominent LREE enrichment and positive Eu anomaly between bulk composition of Hole U1502B (Fig. 5c, d), seafloor venting fluids (Michard et al., 1983; Von Damm et al., 1985; Douville et al., 1999), and high-temperature secondary minerals (Gillis et al., 1992; Fox et al., 2020; Tian et al., 2020). In particular, all the epidote/−rich samples display strong positive Eu anomalies, which may reflect highly oxidized and high-temperature environment in those sections of Hole U1502B (~850–910 m depth: Tian et al., 2020; ~800–830 m depth: this study, also see Supporting Information). These depth ranges (i.e. ~110–170 m and ~60–90 m below Tg) correspond not only to the zonation of epidote + quartz ± chlorite (Figs. S2–S4) that is typical of high-W/R ratio and -temperature conditions (Figs. 3f, j, k, n), but also to the occurrence of chalcopyrite, sphalerite and covellite that are indicative of pulses of hydrothermal activity (Fig. 3b, g).

Taken together, Hole U1502B should have experienced a wide range of hydrothermal environments, representative of those varying from the peripheral, core, to deep parts within an upwelling limb. Such variable environments of discharge zone are consistent with the relative stratigraphy in crust and the alteration migration with rifting, as discussed below.

6.2.2. Relative stratigraphy within crust – mixing zone within lava–dike transition

Hole U1502B well covers the lava section including the upper and lower extrusive rocks, as seen from the lava-flow morphologies of pillow, lobate and massive sheets (Larsen et al., 2018b) (Fig. 2). Even more, Hole U1502B may penetrate through the lava pile to the lava–dike transition, where the temperature is thought to rapidly increase coupled with a large decrease in permeability (cf. Mottl, 1983; Alt, 1995; Coogan, 2008). Within this transition zone, episodic alternate circulation of hot and cold water goes through the same mass of rocks, leading to striking differences in physical properties, geochemical compositions, and mineral assemblages, compared to the overlying lava section (Bickle and Teagle, 1992; Teagle et al., 2003; Heft et al., 2008; Alt et al., 2010; Christeson et al., 2007, 2010).

Seismically, such differences are well reflected in the shipboard data of P-wave velocity and porosity at Site U1502, showing that the boundary of layer 2A/2B corresponds to that of sub-units VIA and VIB (Larsen et al., 2018b; Ding et al., 2020) (Figs. 2 and 11). In general, the seismic structure of upper oceanic crust is divided into layer 1 (<2–3 km/s; sediment), layer 2 (~3–6 km/s; lava & dike), and layer 3 (~6–8 km/s; gabbro); and layer 2 is typically sub-divided further into layers 2A (lava pile), 2B (lava–dike transition), and 2C (sheeted dike) (Harding et al., 1989; Carbotte et al., 1998; Christeson et al., 2007; Gilbert et al., 2018). At Site U1502, the stepwise variations in P-wave velocity not only explicitly indicate the layer 1 (<3 km/s; ~250–750 m depth) and the layer 2 (>3 km/s; >750 m depth), but also permit the layer 2A (~3–4 km/s; lava pile; ~750–800 m depth) and layer 2B (>4 km/s; lava–dike transition; ~800–920 m depth) to be clearly distinguished (Fig. 11b). Similar pattern of downhole changes is also seen from other physical properties acquired at Site U1502, including crustal porosity (Figs. 2 and 11b), bulk density, thermal conductivity, and natural gamma radiation (Larsen et al., 2018b) (see Section 3.1).

Geochemically, several lines of evidence suggest the inferred fluctuating permeability and temperature in the MOR subsurface, pointing to a lava–dike transition for Hole U1502B. These includes: 1) the prominent CaO loss and Na_2O gain caused by intense albitization of calcic plagioclase (Figs. 3b, d, 9a and 10); 2) the positive correlation between the LOI (mainly H_2O contents) and the degree of alteration (as proxied by Ce/Pb), due to formation of secondary hydrous minerals (Figs. 3j, 6a, b, and 8a, b); 3) the conspicuous K_2O decrease and U increase because of retrograde effects (Fig. 9f); and 4) the strong enrichments of base metals (e.g. Zn, Cu, Mn) related to the prevalence of sulfides and Mn-bearing chlorite (Fig. 3h) (cf. Alt et al., 1986; Sleep, 1991; Staudigel et al., 1995; Bach et al., 2003; Nakamura et al., 2007; Barker et al., 2008).

Mineralogically, in the deeper lavas and the underlying sheeted dikes, alteration temperature increase (>100 °C) and most primary igneous phases tend to be entirely replaced by secondary phases (Staudigel, 2014). In Hole U1502B, the mineral assemblage of albite + chlorite + epidote ± quartz ± pyrite in Hole U1502B belongs to the lower greenschist facies (Figs. S2–S4). This alteration phase typically correspond to the depth range between the lava–dike transition and the upper zone of sheeted dike, as widely reported by drilled oceanic crusts and ophiolites (e.g. Alt et al., 1986; Gillis and Robinson, 1990; Gillis and Thompson, 1993; Franzson et al., 2008; Heft et al., 2008; Bach et al., 2013; Staudigel, 2014). In the depth of ~850–890 m, the greenschist facies assemblage were even occasionally overprinted by epidote with minor quartz (Fig. S3), indicating high temperature (~400 °C) and high W/R-ratio (>1) reactions that most likely occurred in/near the reaction zone (Bickle and Teagle, 1992; Gillis et al., 2005; Bach et al., 2013; Humphris and Klein, 2018). This essentially represents an early sign of epidosites and supports a deep stratigraphic depth within curst for Hole U1502B.

6.3. Inferring SCS marginal rifting

deothermal

6.3.1. The nature of layer 2A/2B boundary

Since the layer 2A/2B boundary is seismically ~400–600 m beneath the seafloor in young oceanic crust at various spreading rates (Harding et al., 1989; Carbotte et al., 1998; Christeson et al., 2010), one may argue against the 182-m depth lava–dike transition as inferred for Site U1502. However, drilled hole data and geologic mapping at tectonic windows have shown variable depth to the top of the sheeted dike complex and that there is not a consistent lithologic contact at 400–600 m depth (Christeson et al., 2010; and references therein). There are three possible explanations that are not mutually exclusive.

First, the relatively shallow boundary of layer 2A/2B may be attributed to the nature of slow-spreading, intermediate type of SCS rifted margin (Larsen et al., 2018a; Ding et al., 2020). In fact, a thin lava pile and a thick lava–dike transition (Fig. 11b) are consistent with the magma-poor, hyperextended margin of the northern SCS (Jian et al., 2018; Sun et al., 2018).

Second, this may indicate that the upper parts of Hole U1502B had been emplaced. A gradual downhole increase of predominantly brittle deformation was recorded within the sediments directly overlying the basaltic basement, while severe brecciation was observed for the uppermost ~50 m of the basement (Fig. 2). Such observed deformation structures have been linked to the emplacement history of the basalt and the subsequent development of a hydrothermal system (Larsen et al., 2018b). In this setting, local strain accumulations resulting from possible thermal re-equilibration and triggered by the circulation of hydrothermal fluids in both magmatic rocks and sedimentary cover may be expected (Larsen et al., 2018a, 2018b) (see Section 3.3).

Third, a penetration into the porosity boundary of layer 2A/2B as observed in Site U1502, however, may be simply an alteration front of hydrothermal circulation. Indeed, the geologic context of the layer 2A/2B boundary varies as a result of competing processes, including magmatic construction and fracturing (increasing porosity) and crustal thickening, compaction, dike intrusion, and hydrothermal sealing (decreasing porosity) (Christeson et al., 2007, 2010; Seher et al., 2010; Gilbert et al., 2018; Estep et al., 2019). This would especially be true considering the inferred interaction

to erupt only when plagioclase-bearing magma travel via the conduit systems that lack or bypass shallow AMC (Lange et al., 2013). In fact, the ubiquitous but spare distribution of high-temperature minerals (e.g. albite, chlorite, epidote) in a relatively shallow stratigraphic depth as observed in Hole U1502B (Section 6.2) is consistent with the dike-driven faults and sills that should have promoted the hydrothermal circulation (Sun et al., 2019). These may suggest that the SCS rifted margin was constructed by progressive dike injection, without significant periods of magmatic quenching or enhanced tectonism.

Furthermore, our scenario accounts sufficiently for the differences regarding crustal structure and hydrothermal alteration between Sites U1499, U1500, and U1502 (Figs. 1 and 11). No sign of hydrothermal alteration in Site U1500 can be attributed to enhanced magma supply and volcanic activities at the younger Ridge B, coinciding to the onset of the SCS seafloor spreading (Jian et al., 2018; Sun et al., 2018) (see Section 2). Permeability that was primarily provided by faulting should have been reduced during this magmatic phase; for instance, a lava lake may serve as a barrier to the upwelling fluids.

Besides, the continental affinity found in Site U1499 at the contemporary Ridge A can be explained by the lateral variability caused by tectonic extensions (Fig. 11b), as recently shown by

Alt, J.C., Honnorez, J., Laverne, C., Emmermann, R., 1986. Alteration of a 1-km section through the upper oceanic crust, DSDP Hole 504B: the mineralogy, chemistry, and evolution of basalt-seawater interactions. J. Geophys. Res. 91, 10309–10335.

Alt, J.C., Laverne, C., Coggon, R.M., Teagle, D.A.H., Banerjee, N.R., Morgan, S., Smith-Duque, C.E., Harris, M., Galli, L., 2010. Subsurface structure of a submarine hydrothermal system in ocean crust formed at the East Pacific Rise, ODP/IODP Site 1256. Geochem. Geophys. Geosyst. 11, Q10010 https://doi.org/10.1029/2010GC003144.

Anders, E., Grevesse, N., 1989. Abundances of the elements: meteoritic and solar. Geochim. Cosmochim. Acta 53, 197–214.

Antonelli, M.A., Pester, N.J., Brown, S.T., DePaolo, D.J., 2017. Effect of paleoseawater composition on hydrothermal exchange in midocean ridges. Proc. Natl. Acad. Sci. U. S. A. 114 (47), 12413–12418.

Bach, W., Peucker-Ehrenbrink, B., Hart, S.R., Blusztajn, J.S., 2003. Geochemistry of hydrothermally altered oceanic crust: DSDP/ODP Hole 504B – implications for seawater-crust exchange budgets and Sr- and Pb-isotopic evolution of the mantle. Geochem. Geophys. Geosyst. 4, 8904. https://doi.org/10.1029/2002GC000419.

Bach, W., Jons, J., Klein, F., 2013. Metasomatism with the ocean crust. In: Harlov, D.E., Austrheim, H. (Eds.), Metasomatism and the Chemical Transformation of Rock. Springer, Berlin, pp. 253–288. https://doi.org/10.1007/978-3-642-28394-9_8.

Baker, E.T., 2009. Relationships between hydrothermal activity and axial magma chamber distribution, depth, and melt content. Geochem. Geophys. Geosyst. 10 https://doi.org/10.1029/2009GC002424.

Banerjee, N.R., Gillis, K.M., Muehlenbachs, K., 2000. Discovery of epidosites in a modern oceanic setting, the Tonga forearc. Geology 28, 151–154.

Barker, A.K., Coogan, L.A., Gillis, K.M., Weis, D., 2008. Strontium isotope constraints on fluid flow in the sheeted dike complex of fast spreading crust: pervasive fluid flow at Pito Deep. Geochem. Geophys. Geosyst. 9, Q06010. https://doi.org/10.1029/2007GC001901.

Barker, A.K., Coogan, L.A., Gillis, K.M., Hayman, N.W., Weis, D., 2010a. Direct observation of a fossil high-temperature, fault-hosted, hydrothermal upflow zone in crust formed at the East Pacific Rise. Geology 38, 379–382.

Barker, A.K., Coogan, L.A., Gillis, K.M., 2010b. Insights into the behaviour of sulphur in mid-ocean ridge axial hydrothermal systems from the composition of the sheeted dyke complex at Pito Deep. Chem. Geol. 275, 105–115.

Berndt, M.E., Seyfried Jr., W.E., 1993. Calcium and sodium exchange during hydrothermal alteration of calcic plagioclase at 400°C and 400 Bars. Geochim. Cosmochim. Acta 57, 4445–4451.

Berndt, M.E., Seyfried Jr., W.E., Beck, J.W., 1988. Hydrothermal alteration processes at midocean ridges: experimental and theoretical constraints from Ca and Sr exchange reactions and Sr isotopic ratios. J. Geophys. Res. 93, 4573–4583.

Berndt, M.E., Seyfried Jr., W.E., Janecky, D.R., 1989. Plagioclase and epidote buffering of cation ratios in mid-ocean ridge hydrothermal fluids: experimental results in and near the supercritical region. Geochim. Cosmochim. Acta 53, 2283–2300.

Bickle, M.J., Teagle, D.A.H., 1992. Strontium alteration in the Troodos ophiolite: implications for fluid fluxes and geochemical transport in mid-ocean ridge hydrothermal systems. Earth Planet. Sci. Lett. 113, 219–237.

Bischoff, J.L., Seyfried Jr., W.E., 1978. Hydrothermal chemistry of seawater from 25°C to 350°C. Am. J. Sci. 278, 838–860.

Blundy, J.D., Wood, B.J., 1991. Crystal-chemical controls on the distribution of Sr and Ba between plagioclase feldspar, silicate melts, and hydrothermal solutions. Geochim. Cosmochim. Acta 55, 193–209.

Boschi, C., Früh-Green, G.L., Delacour, A., Karson, J.A., Kelley, D.S., 2006. Mass transfer and fluid flow during detachment faulting and development of an oceanic core complex, Atlantic Massif (MAR 30°N). Geochem. Geophys. Geosyst. 7 https://doi.org/10.1029/2005GC001074.

Briais, A., Patriat, P., Tapponnier, P., 1993. Updated interpretation of magnetic anomalies and seafloor spreading stages in the South China Sea: implications for the Tertiary tectonics of Southeast Asia. J. Geophys. Res. 98, 6299–6328.

Carbotte, S., Mutter, C., Mutter, J., Ponce-Correa, G., 1998. Influence of magma supply and spreading rate on crustal magma bodies and emplacement of the extrusive layer: Insights from the east Pacific rise at lat.16 degrees N. Geology 26, 455–458.

Chauvel, C., Bureau, S., Poggi, C., 2011. Comprehensive chemical and isotopic analyses of basalt and sediment reference materials. Geostand. Geoanal. Res. 35 (1), 125–143.

Christeson, G.L., McIntosh, K.D., Karson, J.A., 2007. Inconsistent correlation of seismic layer 2a and lava layer thickness in oceanic crust. Nature 445, 418–421.

Christeson, G.L., Karson, J.A., McIntosh, K.D., 2010. Mapping of seismic layer 2A/2B boundary above the sheeted dike unit at intermediate spreading crust exposed near the Blanco Transform. Geochem. Geophys. Geosyst. 11, Q03015 https://doi.org/10.1029/2009GC002864.

Clark, C., James, P., 2003. Hydrothermal brecciation due to fluid pressure fluctuations: examples from the Olary Domain, South Australia. Tectonophysics 366 (3–4), 187–206.

Coogan, L.A., 2008. Reconciling temperatures of metamorphism, fluid fluxes, and heat transport in the upper crust at intermediate to fast spreading mid-ocean ridges. Geochem. Geophys. Geosyst. 9, Q02013.

Coogan, L.A., Gillis, K.M., 2018. Low-temperature alteration of the seafloor: impacts on ocean chemistry. Annu. Rev. Earth Planet. Sci. 46, 21–45.

Cullen, A., Vicenzi, E., Mcbirney, A.R., 1989. Plagioclase-ultraphyric basalts of the Galapagos Archipelago. J. Volcanol. Geotherm. Res. 37, 325–337.

Dai, B., Jiang, S., Jiang, Y., Zhao, K., Liu, D., 2008. Geochronology, geochemistry and Hf–Sr–Nd isotopic compositions of Huziyan mafic xenoliths, southern Hunan Province, South China: petrogenesis and implications for lower crust evolution. Lithos 102, 65–87.

Delacour, A., Fruh-Green, G.L., Frank, M., Gutjahr, M., Kelley, D.S., 2008. Sr- and Nd-isotope geochemistry of the Atlantis Massif (30°N, MAR): implications for fluid fluxes and lithospheric heterogeneity. Chem. Geol. 254, 19–35.

Delaney, J.R., Mogk, D.W., Mottl, M.J., 1987. Quartz-cemented breccias from the Mid-Atlantic Ridge: samples of a high-salinity hydrothermal upflow zone. J. Geophys. Res. 92, 9174–9192.

Ding, K., Seyfried Jr., W.E., 1994. Effect of conductive cooling on chemistry of mid-ocean ridge hydrothermal fluids: experimental and theoretical constraints. Mineral. Mag. episodically–232. oceanic epizoned

Ding, W.W., Sun, Z., Mohn, G., Nirrengarten, M., Tugend, J., Manatschal, G., Li, J.B., 2020. Lateral evolution of the rift-to-drift transition in the South China Sea: evidence from multi-channel seismic data and IODP Expeditions 367&368 drilling results. Earth Planet. Sci. Lett. 531, 115932.

Douville, E., Bienvenu, P., Charlou, J.L., Donval, J.P., Fouquet, Y., Appriou, P., Gamo, T., 1999. Yttrium and rare earth elements in fluids from various deep-sea hydrothermal systems. Geochim. Cosmochim. Acta 63, 627–643.

Escartín, J., Smith, D.K., Cann, J., Schouten, H., Langmuir, C.H., Escrig, S., 2008. Central role of detachment faults in accretion of slow-spreading oceanic lithosphere. Nature 455, 790–795.

Estep, J., Reece, R., Kardell, D.A., Christeson, G.L., Carlson, R.L., 2019. Seismic Layer 2A: evolution and thickness from 0 to 70 Ma crust in the slow-intermediate spreading South Atlantic. J. Geophys. Res. Solid Earth 124, 7633–7651.

Fan, C.Y., Xia, S.H., Cao, J.H., Zhao, F., Sun, J.L., Wan, K.Y., Xu, H.L., 2019. Lateral crustal variation and post-rift magmatism in the northeastern South China Sea determined by wide-angle seismic data. Mar. Geol. 410, 70–87.

Flower, M.F.J., 1980. Accumulation of calcic plagioclase in ocean-ridge tholeiite: an indication of spreading rate. Nature 287, 530–532.

Fowler, A.P.G., Zierenberg, R.A., 2016. Elemental changes and alteration recorded sitg geothermal the Geophys.

ridges: evidence from the sheeted dike complex at Pito Deep. Geochem. Geophys. Geosyst. 9, Q05007 https://doi.org/10.1029/2007GC001926.

Hofmann, A.W., Jochum, K.P., Seufert, M., White, W.M., 1986. Nb and Pb in oceanic basalts: new constraints on mantle evolution. Earth Planet. Sci. Lett. 79, 33–45.

Huang, C.Y., Wang, P.X., Yu, M.M., You, C.F., Liu, C.S., Zhao, X.X., Shao, L., Zhong, G.F., Yumul, G.P., 2019. Potential role of strike-slip faults in opening up the South China Sea. Natl. Sci. Rev. 6, 891–901.

Humphris, S.E., Klein, F., 2018. Progress in deciphering the controls on the geochemistry of fluids in seafloor hydrothermal systems. Annu. Rev. Mar. Sci. 10, 315–343.

Humphris, S.E., Thompson, G., 1978. Hydrothermal alteration of oceanic basalts by seawater. Geochim. Cosmochim. Acta 42, 107–125.

Jébrak, M., 1997. Hydrothermal breccias in vein-type ore deposits: a review of mechanisms, morphology and size distribution. Ore Geol. Rev. 12, 111–134.

Jian, Z.M., Larsen, H.C., Alvarez Zarikian, C.A., The Expedition 368 Scientists, 2018. Expedition 368 Preliminary Report: South China Sea Rifted Margin. International Ocean Discovery Program Preliminary Report, 368. https://doi.org/10.14379/iodp.pr.368.2018.

Jian, Z.M., Jin, H.Y., Kaminski, M.A., Ferreira, F., Li, B.H., Yu, P.S., 2019. Discovery of the marine Eocene in the northern South China Sea. Natl. Sci. Rev. 6, 881–885.

Kawahata, H., Nohara, M., Ishizuka, H., Hasebe, S., Chiba, H., 2001. Sr isotope geochemistry and hydrothermal alteration of the Oman ophiolite. J. Geophys. Res. Solid Earth 106, 11083–11099.

Kennish, M.J., Lutz, R.A., 1998. Morphology and distribution of lava flows on mid-ocean ridges: a review. Earth Sci. Rev. 43, 63–90.

Klinkhammer, G.P., Elderfield, H., Edmond, J.M., Mitra, A., 1994. Geochemical implications of rare earth element patterns in hydrothermal fluids from mid-ocean ridges. Geochim. Cosmochim. Acta 58, 5105–5113.

Labanieh, S., Chauvel, C., Germa, A.l., Quidelleur, X., 2012. Martinique: a clear case for sediment melting and slab dehydration as a function of distance to the Trench. J. Petrol. 53 (12), 2441–2464.

Lange, A.E., Nielsen, R.L., Tepley, F.J., Kent, A.J.R., 2013. The petrogenesis of plagioclase-phyric basalts at mid-ocean ridges. Geochem. Geophys. Geosyst. 14, 3282–3296.

Larsen, H.C., Mohn, G., Nirrengarten, M., Sun, Z., Stock, J., Jian, Z., IODP Expeditions 367/368 Scientists, 2018a. Rapid transition from continental breakup to igneous oceanic crust in the South China Sea. Nat. Geosci. 11, 782–789.

Larsen, H.C., Jian, Z., Alvarez Zarikian, C.A., Sun, Z., Stock, J.M., Klaus, A., The Expeditions 367/368 Scientists, 2018b. Site U1502. In: Sun, Z., Jian, Z., Stock, J.M., Larsen, H.C., Klaus, A., Zarikian, C.A. Alvarez, the Expeditions 367/368 Scientists (Eds.), South China Sea Rifted Margin – Proceedings of the International Ocean Discovery Program. International Ocean Discovery Program, College Station, TX. https://doi.org/10.14379/iodp.proc.367368.106.2018 (vols. 367/368, CH. 6).

Lester, R., Van Avendonk, H.J.A., McIntosh, K., Lavier, L., Liu, C.S., Wang, T.K., Wu, F., 2014. Rifting and magmatism in the northeastern South China Sea from wide-angle tomography and seismic reflection imaging. J. Geophys. Res. Solid Earth 119, 2305–2323.

Li, C.F., Xu, X., Lin, J., Sun, Z., Zhu, J., Yao, Y.J., IODP Expedition 349 Scientists, 2014. Ages and magnetic structures of the South China Sea constrained by deep tow magnetic surveys and IODP Expedition 349. Geochem. Geophys. Geosyst. 15, 4958–4983.

Li, C.F., Li, J.B., Ding, W.W., Franke, D., Yao, Y.J., IODP Expedition 349 Scientists, 2015. Seismic stratigraphy of the central South China Sea basin and implications for neotectonics. J. Geophys. Res. Solid Earth 120, 1377–1399.

Ligi, M., Bonatti, E., Bortoluzzi, G., Cipriani, A., Cocchi, L., Tontini, F.C., Carminati, E., Ottolini, L., Schettino, A., 2012. Birth of an ocean in the Red Sea: initial pangs. Geochem. Geophys. Geosyst. 13, Q08009 https://doi.org/10.1029/2012GC004155.

Liu, Z.F., Li, C.F., Kulhanek, D., 2017. Preface: Evolution of the deep South China Sea: integrated IODP Expedition 349 results. Mar. Geol. 394, 1–3.

Lizarralde, D., Axen, G.J., Brown, H.E., Fletcher, J.M., González-Fernández, A., Harding, A.J., Holbrook, W.S., Kent, G.M., Paramo, P., Sutherland, F., Umhoefer, P. J., 2007. Variation in styles of rifting in the Gulf of California. Nature 448, 466–469.

Macdonald, G.A., Katsura, T., 1964. Chemical composition of Hawaiian lavas. J. Petrol. 5, 82–133.

McArthur, J.M., Howarth, R.J., Shields, G.A., 2012. Strontium isotope stratigraphy. In: Gradstein, F.M., Ogg, J.G., Schmitz, M., Ogg, G. (Eds.), The Geologic Time Scale 2012. Elsevier, Amsterdam, pp. 127–144. https://doi.org/10.1016/B978-0-444-59425-9.00007-X. CH. 6.

McCaig, A.M., Cliff, R.A., Escartín, J., Fallick, A.E., MacLeod, C.J., 2007. Oceanic detachment faults focus very large volumes of black smoker fluids. Geology 35, 935–938.

Michard, A., Albarède, F., 1986. The REE content of some hydrothermal fluids. Chem. Geol. 55, 51–60.

Michard, A., Albarède, F., Michard, G., Minster, J.F., Charlou, J.L., 1983. Rare-earth elements and uranium in high-temperature solutions from East Pacific Rise hydrothermal vent field (13°N). Nature 303, 795–797.

Mottl, M.J., 1983. Metabasalts, axial hot springs and the structure of hydrothermal systems at mid-ocean ridges. Geol. Soc. Am. Bull. 94, 161–180.

Mottl, M.J., Seewald, J.S., Wheat, C.G., Tivey, M.K., Michael, P.J., Proskurowski, G., McCollom, T.M., Reeves, E., Sharkey, J., You, C.F., Chan, L.H., Pichler, T., 2011. Chemistry of

Tolstoy, M., Waldhauser, F., Bohnenstiehl, D.R., Weekly, R.T., Kim, W.Y., 2008. Seismic identification of along-axis hydrothermal flow on the East Pacific Rise. Nature 451, 181–187.

Von Damm, K.L., Edmond, J.M., Grant, B., Measures, C.I., Walden, B., Weiss, R.F., 1985. Chemistry of submarine hydrothermal solutions at 21°N, East Pacific Rise. Geochim. Cosmochim. Acta 49, 2197–2220.

Von Damm, K.L., Oosting, S.E., Kozlowski, R., Buttermore, L.G., Colodner, D.C., 1995. Evolution of East Pacific Rise hydrothermal vent fluids following volcanic eruption. Nature 375, 47–50.

Wang, P., Huang, C.-Y., Lin, J., Jian, Z., Sun, Z., Zhao, M., 2019. The South China Sea is not a mini-Atlantic: plate-edge rifting vs intra-plate rifting. Natl. Sci. Rev. 6 (5), 902–913.

Whitmarsh, R.B., Manatschal, G., Minshull, T., 2001. Evolution of magma-poor continental margins from rifting to seafloor spreading. Nature 413, 150–154.

Wu, J.W., Filippidi, A., Davies, G.R., de Lange, G.J., 2018. Riverine supply to the eastern Mediterranean during last interglacial sapropel S5 formation: a basin-wide perspective. Chem. Geol. 485, 74–89.

Yu, X., Liu, Z.F., 2020. Non-mantle-plume process caused the initial spreading of the South China Sea. Sci. Rep. 10, 8500. https://doi.org/10.1038/s41598-020-65174-y.

Zhang, G.L., Luo, Q., Zhao, J., Jackson, M.G., Guo, L.S., Zhong, L.F., 2018. Geochemical nature of sub-ridge mantle and opening dynamics of the South China. Earth Planet. Sci. Lett. 489, 145–155.

Zhao, F., Alves, T.M., Xia, S.H., Li, W., Wang, L., Mi, L.J., Wu, S.G., Cao, J.H., Fan, C.Y., 2020. Along-strike segmentation of the South China Sea margin imposed by inherited pre-rift basement structures. Earth Planet. Sci. Lett. 530, 115862.

Zhong, L.F., Cai, G.Q., Koppers, A.A.P., Xu, Y.G., Xu, H.H., Gao, H.F., Xia, B., 2018. $^{40}Ar/^{39}Ar$ dating of oceanic plagiogranite: constraints on the initiation of seafloor spreading in the South China Sea. Lithos 302, 421–426.